Nano Research
2023, 16(2): 2859–2865

ISSN 1998-0124 CN 11-5974/O4
https://doi.org/10.1007/s12274-022-5005-z

Research Article

Ratiometric fluorescent Si-FITC nanoprobe for immunoassay of SARS-CoV-2 nucleocapsid protein

Guobin Mao[1,§], Silu Ye[1,2,§], Wen Yin[2], Yang Yang[3], Xinghu Ji[4], Jin He[2], Yingxia Liu[3], Junbiao Dai[1], Zhike He[4] (✉), and Yingxin Ma[1] (✉)

[1] *CAS Key Laboratory of Quantitative Engineering Biology, Guangdong Provincial Key Laboratory of Synthetic Genomics and Shenzhen Key Laboratory of Synthetic Genomics, Shenzhen Institute of Synthetic Biology, Shenzhen Institutes of Advanced Technology, Chinese Academy of Sciences, Shenzhen 518055, China*

[2] *State Key Laboratory of Agricultural Microbiology, College of Life Science and Technology, Huazhong Agricultural University, Wuhan 430070, China*

[3] *Shenzhen Key Laboratory of Pathogen and Immunity, National Clinical Research Center for Infectious Disease, State Key Discipline of Infectious Disease, Shenzhen Third People's Hospital, Second Hospital Affiliated to Southern University of Science and Technology, Shenzhen 518112, China*

[4] *College of Chemistry and Molecular Sciences, Wuhan University, Wuhan 430072, China*

[§] *Guobin Mao and Silu Ye contributed equally to this work.*

Received: 4 July 2022 / **Revised:** 31 August 2022 / **Accepted:** 1 September 2022

ABSTRACT

Coronavirus disease 2019 (COVID-19) highlights the importance of rapid and reliable diagnostic assays for the management of virus transmission. Here, we developed a one-pot hydrothermal method to prepare Si-FITC nanoparticles (NPs) for the fluorescent immunoassay of severe acute respiratory syndrome coronavirus 2 (SARS-CoV-2) nucleocapsid protein (N protein). The synthesis of Si-FITC NPs did not need post-modification, which addressed the issue of quantum yield reduction during the coupling reaction. Si-FITC NPs showed two distinct peaks, Si fluorescence at λ_{em} = 385 nm and FITC fluorescence at λ_{em} = 490 nm. In the presence of $KMnO_4$, Si fluorescence was decreased and FITC fluorescence was enhanced. Briefly, in the presence of N protein, catalase (CAT)-linked secondary antibody/reporter antibody/N protein/capture antibody immunocomplexes were formed on microplates. Subsequently, hydrogen peroxide (H_2O_2) and Si-FITC NPs/$KMnO_4$ were injected into the microplate together. The decomposition of H_2O_2 by CAT resulted in remaining of $KMnO_4$, which changed the fluorescence intensity ratio of Si-FITC NPs. The fluorescence intensity ratio correlated significantly with the N protein concentration ranging from 0.02 to 50.00 ng/mL, and the detection limit was 0.003 ng/mL, which was more sensitive than the commercial ELISA kit with a detection limit of 0.057 ng/mL. The N protein concentration can be accurately determined in human serum. Furthermore, the COVID-19 and non-COVID-19 patients were distinguishable by this method. Therefore, the ratiometric fluorescent immunoassay can be used for SARS-CoV-2 infection diagnosis with a high sensitivity and selectivity.

KEYWORDS

Si-FITC nanoparticles, ratiometric fluorescent probe, SARS-CoV-2, ELISA

1 Introduction

Coronavirus disease 2019 (COVID-19) was caused by the severe acute respiratory syndrome coronavirus 2 (SARS-CoV-2) [1, 2]. By April 2022, over 500 million cases of SARS-CoV-2 infections had been identified worldwide, posing a major threat to human health and leading to huge economic losses. The COVID-19 pandemic highlights the importance of rapid and reliable diagnostic techniques to control and prevent virus transmission [3–5]. Nucleic acids, antibodies, and antigens are considered as common targets for the diagnosis of viral diseases. Nucleic acid-based assay, which is highly sensitive and specific, is widely accepted as the gold standard for the detection of RNA viruses. The common methods include quantitative real-time PCR (RT-qPCR) [6, 7], high-throughput gene sequencing [8], loop-mediated isothermal amplification (LAMP) [9, 10], and CRISPR-based assays [11–13]. However, the application of nucleic acid-based methods is still limited by some disadvantages, such as the requirement of skilled technicians, complicated equipment, time-consuming procedures, and high false-positive rate [14]. In contrast, antibody/antigen-based tests are easy to operate, and do not require extensive technical expertise and expensive instruments [15, 16]. Nevertheless, the long window period restricts the application of antibody detection for early diagnosis of infections [17, 18]. Antigen detection test has become a direct and rapid method for early identification of virus infections [19, 20].

As a classical immunoassay, enzyme-linked immunosorbent assay (ELISA) combines the high specificity of the antibody-antigen binding and the high-conversion catalytic effect of enzymes to amplify the detection signal [21, 22]. ELISA has been widely used in clinical diagnosis, food safety, and environmental monitoring due to its high-throughput detections, easy

Address correspondence to Yingxin Ma, yx.ma1@siat.ac.cn; Zhike He, zhkhe@whu.edu.cn

procedures, and low costs [23, 24]. Colorimetric and fluorescent methods are the most commonly used assays in ELISA. Fluorescence detection achieves a higher sensitivity and better selectivity than colorimetric detection [25], and a fluorescent ELISA was developed to detect ochratoxin A through the fluorescence quenching of CdTe quantum dots mediated by glucose oxidase-catalysis [26]. Due to better biocompatibility, lower photo-bleaching, and higher abundance [27–29], silicon nanoparticles (Si NPs) have been used to construct fluorescent ELISA systems for the detection of alpha-fetoprotein and human immunoglobulin G [30]. In these analytical methods, single-emission probes are susceptible to environmental changes and concentration fluctuations [30, 31]. By contrast, ratiometric fluorescent probes can effectively reduce the interference caused by external fluctuations, and provide a higher signal-to-noise ratio and better accuracy [32–34].

In this study, we developed a simple one-pot hydrothermal method to prepare silicon-fluorescein isothiocyanate (Si-FITC) NPs for detection of SARS-CoV-2 nucleocapsid protein (N protein) by fluorescent immunoassay. (3-aminopropyl) triethoxysilane (APTES) and APTES-FITC were used as Si co-sources to prepare Si-FITC NPs, and APTES-FITC was prepared by the coupling reaction of the isothiocyanate group of FITC with the amino group of APTES (Scheme 1(a)). The synthesis of Si-FITC NPs did not need post-modification, which addressed the issue of quantum yield reduction. Si-FITC NPs showed two distinct peaks, Si fluorescence at 385 nm and FITC fluorescence at 490 nm. The Si-FITC NPs can be used as a ratiometric fluorescence probe for immunoassay of N protein (Scheme 1(b)). In the presence of $KMnO_4$, Si fluorescence was decreased and FITC fluorescence was enhanced. Briefly, in the presence of N protein, catalase (CAT)-linked secondary antibody/reporter antibody/N protein/capture antibody immunocomplexes were formed on microplate. Subsequently, hydrogen peroxide (H_2O_2) and Si-FITC NPs/$KMnO_4$ were injected into the microplate. The decomposition of H_2O_2 by CAT resulted in remaining of $KMnO_4$, which changed the fluorescence intensity ratio of Si-FITC NPs. The fluorescence intensity ratio correlated significantly with the N protein concentration ranging from 0.02 to 50.00 ng/mL, and the detection limit was 0.003 ng/mL, which was more sensitive than the commercial ELISA kit with a detection limit of 0.057 ng/mL. The N protein concentration can be accurately determined in human serum. Furthermore, this method can accurately distinguish COVID-19 and non-COVID-19 patients. Therefore, the ratiometric fluorescent immunoassay seems effective for diagnosis of SARS-CoV-2 infections with a good sensitivity and selectivity.

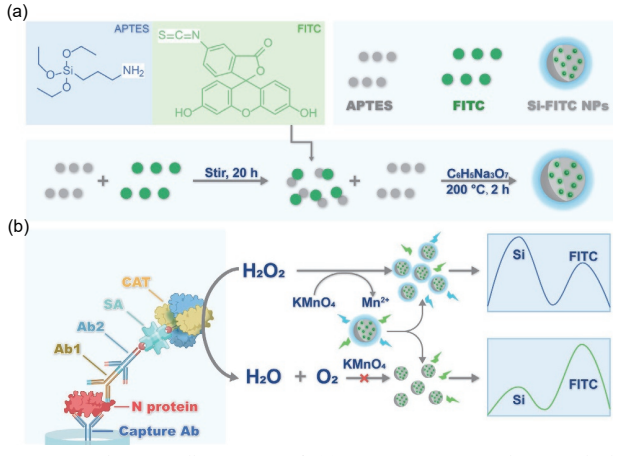

Scheme 1 Schematic illustrations of (a) Si-FITC NPs synthesis and (b) ratiometric immunoassay of SARS-CoV-2 N protein.

2 Experimental

2.1 Chemicals and materials

Trizma hydrochloride (Tris-HCl), sodium citrate tribasic dihydrate, APTES, FITC isomer, dimethyl sulfoxide (DMSO), NHS-dPEG$_4$-biotin, bovine serum albumin, CAT from bovine liver, glutamic acid, threonine, proline, serine, valine, tyrosine, $CaCl_2$, KCl, $ZnAc_2$, and $MgCl_2$ were purchased from Sigma (St. Louis, MO, USA). SARS-CoV-2 N protein-His recombinant protein, mouse anti-SARS-CoV-2 N protein mAb, rabbit anti-SARS-CoV-2 N protein monoclonal antibody, and SARS-CoV-2 nucleocapsid detection ELISA kit were provided by Sino Biological, Inc. (Beijing, China). $KMnO_4$, $FeSO_4$, and $MnSO_4$ were provided by Sinopharm Chemical Reagent Co., Ltd. (Shanghai, China). $FeCl_3$ was obtained from ACROS Organics (Geel, Belgium). $CuCl_2$ was purchased from Alfa Aesar (Bethesda, MD, USA). NH_4Cl was provided by Xilong Chemical Co., Ltd (Shantou, China). Hydrogen peroxide was provided by Shanghai Lingfeng Chemical Reagent Co., Ltd. (Shanghai, China). Biotinylated goat anti-rabbit secondary antibody was purchased from Beyotime Biotechnology (Shanghai, China).

2.2 Instruments and characterization

Transmission electron microscopy (TEM) images were obtained on the JEM 2100 microscope (JEOL Ltd., New York, NY, China). X-ray diffraction (XRD) spectra were recorded using the Ultima IV XRD system (Rigaku, Tokyo, China). Cary 3500 UV–vis absorption spectra were obtained using Agilent (Santa Clara, CA, USA). X-ray photoelectron spectroscopy (XPS) was performed on the K-alpha spectrometer (Thermo Scientific, Waltham, MA, USA). Fourier transform infrared (FT-IR) spectra were recorded using the IRAffinity-1s spectrometer (Shimadzu, Kyoto, Japan). Synchronous fluorescence spectra were measured using the F-4700 FL spectrophotometer (Hitachi, Kyoto, Japan). Time-resolved fluorescence spectra were collected using the Edinburgh FLS1000 (Edinburgh Instruments, Fulton, MD, USA).

2.3 Synthesis and purification of Si-FITC NPs

For the preparation of Si-FITC NPs, FITC was covalently coupled with APTES. In a flask, 0.404 g FITC was dissolved with 5 mL ethanol, and 0.2 mL APTES was added into the above mentioned solution. The reaction mixture was protected from light and nitrogen and stirred for 20 h to obtain FITC-APTES. Subsequently, Si-FITC NPs were synthesized by a one-pot hydrothermal method for which 0.184 g trisodium citrate was dissolved in 4 mL ultrapure water in a flask, and 1 mL APTES and 0.1 mL FITC-APTES were added into the above mixture. The reaction solution was stirred for 5 min, transferred to a Teflon-lined stainless-steel autoclave, and reacted at 200 °C for 2 h. Then, the crude product was purified using acetonitrile. The Si-FITC NPs were mixed with acetonitrile at a ratio of 1:4 and centrifuged at 8,000 r/min for 15 min. The supernatant was discarded, and the remaining solution was vacuum-dried overnight at 60 °C to obtain Si-FITC NPs as crystals. The stock solution was prepared by dissolving the purified Si-FITC NPs in 1 mL of deionized water to prepare a Si-FITC NP solution (50 mg/mL) and stored at 4 °C for subsequent uses.

2.4 Effect of $KMnO_4$, H_2O_2, and CAT on the fluorescence of Si-FITC NPs

The fluorescence response of Si-FITC NPs to $KMnO_4$ was investigated by mixing 4 μL Si-FITC NPs with different concentrations of $KMnO_4$ in Tris-HCl buffer (pH 8.0, 20 mM).

Synchronous fluorescence spectra were collected with the excitation wavelength from 350 to 600 nm, and with $\Delta\lambda$ of 30 nm. The fluorescence response of the Si-FITC NPs-$KMnO_4$ system to H_2O_2 was similarly investigated by mixing different concentrations of H_2O_2 in Tris-HCl buffer (20 mM, pH 8.0) with 50 μM $KMnO_4$. Following reaction for 30 min, 4 μL Si-FITC NPs was added, and synchronous fluorescence spectra were obtained. For investigating the fluorescence response of the Si-FITC NPs-$KMnO_4$-H_2O_2 system to CAT, different concentrations of CAT in Tris-HCl buffer (pH 8.0, 20 mM) were mixed with $KMnO_4$ and H_2O_2, and finally, Si-FITC NPs were added, and synchronous fluorescence spectra were recorded.

2.5 Preparation of biotin-CAT conjugates

CAT and NHS-dPEG$_4$-biotin were mixed in 1 mL PBS (10 mM, pH 8.0) with a mole ratio of 1:100 and shaken at 37 °C for 4 h to obtain biotin-CAT. Then, the reaction solution was purified by centrifuging at 8,000 r/min for 10 min with a pore size of 30 kDa. This step of filtration was repeated thrice using deionized water. The conjugation of NHS-dPEG$_4$-biotin and CAT was verified using SA-coated magnetic beads for separating biotin-CAT (37 °C, 30 min). The CAT activity of the supernatant was measured by the Si-FITC NPs/$KMnO_4$/H_2O_2 system.

2.6 N protein detection using ELISA with Si-FITC NPs

Each well was coated with 100 mL of capture antibody (mouse monoclonal antibody, 1:200) in carbonate buffer (50 mM, pH 9.6) at 4 °C overnight. After removing the carbonate buffer and washing thrice with washing buffer (PBS containing 0.05% Tween 20, pH 7.4, 10 mM), the wells were blocked with 2.5% skimmed milk (300 μL) for 2 h at 37 °C and washed thrice with washing buffer. Then, different concentrations of N protein (0, 0.02, 0.05, 0.1, 0.5, 1.0, 10, 20, 40, and 50 ng/mL) were incubated for 1 h at 37 °C to form the capture antibody-N protein complex and washed thrice with washing buffer. The reporter antibody (rabbit monoclonal antibody, 1:5,000; 100 μL) was incubated with the above mixture for 1 h at 37 °C to form a sandwiched immunocomplex, which was then washed thrice with washing buffer. Subsequently, biotin-antibody 2 (biotinylated goat anti-rabbit antibody, 1:2,000; 100 μL) was incubated with the above mixture for 1 h at 37 °C and washed thrice with washing buffer. Each well was added with 100 μL of SA (2.5 μg/mL), incubated at 37 °C for 30 min and washed thrice with washing buffer. Then, biotin-CAT (1:100; 100 μL) was added, incubated at 37 °C for 30 min, and washed thrice with washing buffer. Finally, H_2O_2 in Tris-HCl buffer (pH 7.0, 20 mM) was added to each well and reacted at 30 °C for 1 h. The above solutions were transferred from the well plate to 1.5 mL centrifuge tubes containing the Si-FITC NPs/$KMnO_4$/H_2O_2 system, and synchronous fluorescence spectra were recorded. SARS-CoV-2 N protein was detected using commercial SARS-CoV-2 N protein ELISA kits for sensitivity comparison. To investigate the performance of ratiometric ELISA in serum, different concentrations of N protein was spiked into 100% human serum, and the serum sample containing N protein was added to the wells and detected by the above ELISA assay.

2.7 Analysis of clinical samples

All clinical samples were provided by Shenzhen Third People's Hospital, and laboratory confirmed using quantitative real-time PCR kits for SARS-CoV-2. The samples were inactivated by heating at 56 °C for 30 min and stored at −80 °C until subsequent uses. 9 positive samples and 5 negative samples were lysed with lysis buffer for 15 min, and diluted with PBS, with a total volume of 200 μL. The samples were detected using this proposed method described above.

3 Results and discussion

3.1 Synthesis and characterization of Si-FITC NPs

Si-FITC NPs were synthesized (Scheme 1(a)). APTES-FITC was obtained by reaction of the isothiocyanate group of FITC with the amino group of APTES. Si-FITC NPs were synthesized by one-pot hydrothermal route using trisodium citrate as a reducing agent and APTES/APTES-FITC as a Si co-source. The UV–vis absorption spectra of the prepared Si-FITC NPs were obtained (Fig. 1(a)). Two distinct peaks of Si-FITC NPs were observed at 240 nm and 488 nm, which were attributed to FITC. In addition, an absorption peak was also observed at 260 nm in Si-FITC NPs, which was similar to free Si NPs. The synchronous fluorescence spectra of Si-FITC NPs revealed a fluorescence peak of Si at 385 nm and a FITC fluorescence peak at 490 nm, respectively (Fig. 1(b)). These results preliminarily indicated that FITC was conjugated with Si in the prepared nanoparticles. The excitation spectrum of FITC was partly overlapped with the emission spectrum of Si NPs (Fig. S1(a) in the Electronic Supplementary Material (ESM)), which probably induced the energy transfer from Si NPs to FITC. The fluorescence lifetime of Si NPs and Si in Si-FITC NPs was measured for further investigation of energy transfer. The lifetime of Si in Si-FITC NPs (8.71 ns) was smaller than that of Si NPs (9.58 ns), which was probably attributed to energy transfer from Si to FITC and the transfer efficiency was 9.08% (Fig. S1(b) in the ESM). The energy transfer efficiency was low and had few effects on subsequent detection experiments.

The morphology, size, and crystal structure of Si-FITC NPs were investigated by TEM. Si-FITC NPs were spherical with good mono-dispersity (Fig. 2(a)), and Si-FITC NPs had an average diameter of 1.6 nm (Fig. 2(a) insert). An obvious crystal structure was observed in the HR-TEM images, demonstrating high crystallinity of the prepared Si-FITC NPs. FTIR spectroscopy recorded in the range of 500 to 4,000 cm^{-1} had a strong absorption peak at 1,030 cm^{-1} (stretching vibration of Si–O), an absorption peak at 1,588 cm^{-1} (bending vibration of N–H), and absorption peaks at 2,931 cm^{-1} and 3,356 cm^{-1} (stretching vibration of O–H and N–H), suggesting that the amino group was located on the surface of Si-FITC NPs (Fig. 2(b)). In addition, the absorption peak at 2,028 cm^{-1} attributed to –SCN in FITC disappeared after the preparation Si-FITC NPs, firstly indicating the reaction of –SCN in FITC with –NH_2 in APTES (Fig. S2 in the ESM). XRD spectra showed that Si-FITC NPs had an obvious diffraction peak at 23 degrees. It was not significantly different from the diffraction peak of Si NPs (Fig. 2(c)). XRD analysis displayed no effect on the crystal structure of nanoparticles, and XPS showed that Si2p, S2p, C1s, N1s, and O1s were distributed on the solid surface of Si-FITC NPs (Fig. 2(d)). To further demonstrate the conjugation of FITC and Si in nanoparticles, the HRXPS of C1s in Si NPs and Si-FITC NPs was measured. The percentage of O–C=O in Si-FITC NPs was more than that in Si NPs (Fig. S3 in the ESM), which was probably due to the –COOH in FITC, indicating the coupling reaction of –SCN of FITC with –NH_2 of APTES.

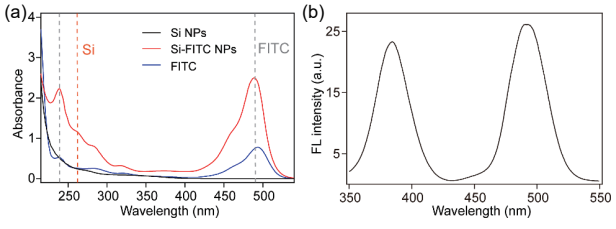

Figure 1 Spectral characterization of Si-FITC NPs. (a) UV–vis absorption spectra of Si NPs, Si-FITC NPs, and free FITC. Si NPs, 1 mg/mL; Si-FITC NPs, 1 mg/mL; FITC, 5 μg/mL. (b) Synchronous fluorescence spectra of Si-FITC NPs. λ_{ex} = 350 to 550 nm, $\Delta\lambda$ = 30 nm.

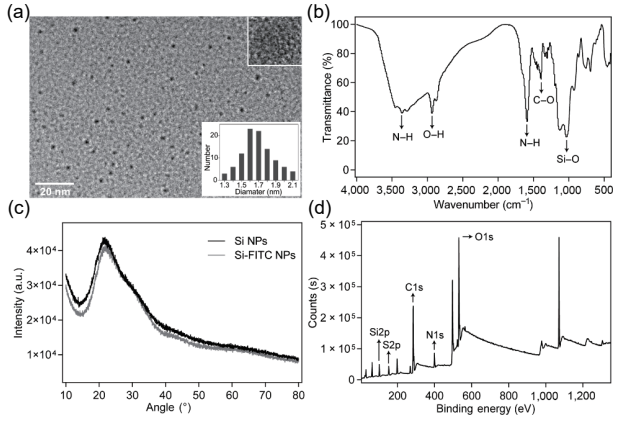

Figure 2 Elemental composition and structural characterization of Si-FITC NPs. (a) TEM image, insert: HR-TEM image and size distribution histogram. (b) FTIR spectrum. (c) XRD spectra of Si NPs and Si-FITC NPs. (d) XPS spectrum.

3.2 Stability analysis of Si-FITC NPs

The photostability of Si-FITC NPs was studied by continuously exposing them to 350 V excitation radiation for 2 h. The fluorescence intensity of Si in Si-FITC NPs remained at 80%, and the fluorescence intensity of FITC in Si-FITC NPs exceeded 100% (Fig. 3(a)). The fluorescence intensity of free FITC was only 50% after 2 h of excitation radiation. Both Si and FITC in Si-FITC NPs possessed a good photostability. Due to the protective effect of nano-coating, the photostability of FITC in Si-FITC NPs was much higher than that of free FITC. The pH stability of Si-FITC NPs was investigated using Tris-HCl buffer with pH 4 to 12. Free FITC was sensitive to pH change, and the fluorescence intensity of FITC increased significantly with the pH from 5 to 9 (Fig. S4 in the ESM). In contrast, Si-FITC NPs showed an ideal pH stability, and the fluorescence intensity ratio (F_{385}/F_{490}) changed slightly from pH 4 to 12 (Figs. 3(b) and 3(c)). Combined with these two results, we predicted that FITC was located inside Si-FITC NPs rather than on the surface of nanoparticles. The blocking of FITC by Si coating made the ratiometric probe have better photostability and wider pH stability range, and have excellent potential as a long-term imaging probe. The anti-interference ability of Si-FITC NPs was also tested with ions, amino acids, and protein commonly existing in body fluids, including Mn^{2+}, Cu^{2+}, Ca^{2+}, K^+, Zn^{2+}, NH_4^+, Mg^{2+}, Glu, Thr, Pro, Ser, Val, Tyr, glucose, and BSA. The concentration of the above ions, amino acids and glucose was 100 μM and that of BSA was 1 μM. The change of fluorescence ratio was negligible, indicating that Si-FITC NPs had excellent anti-interference ability (Fig. 3(d)).

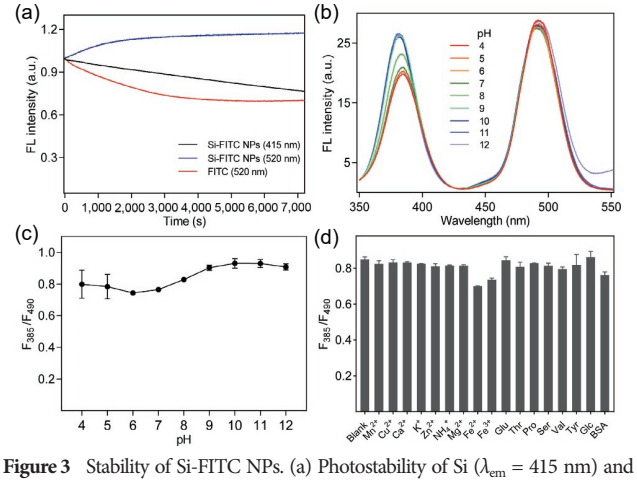

Figure 3 Stability of Si-FITC NPs. (a) Photostability of Si (λ_{em} = 415 nm) and FITC (λ_{em} = 520 nm) in Si-FITC NPs, and free FITC (λ_{em} = 520 nm). (b) Synchronous fluorescence spectra and (c) fluorescence intensity ratio of Si-FITC NPs in Tris-HCl buffer at different pH values. $\Delta\lambda$ = 30 nm. (d) Anti-interference ability of Si-FITC NPs against Mn^{2+} ($MnSO_4$), Cu^{2+} ($CuCl_2$), Ca^{2+} ($CaCl_2$), K^+ (KCl), Zn^{2+} ($ZnAc_2$), NH_4^+ (NH_4Cl), Mg^{2+} ($MgCl_2$), Fe^{2+} ($FeSO_4$), Fe^{3+} ($FeCl_3$), glutamic acid, threonine, proline, serine, valine, tyrosine, glucose and BSA. The concentration of the above ions, amino acids and glucose was 100 μM and that of BSA was 1 μM.

3.3 Effects of $KMnO_4$ and H_2O_2 on the Si-FITC NPs

The effect of $KMnO_4$ on Si-FITC NPs fluorescence was measured at different concentrations of $KMnO_4$ (0 to 200 μM). In our system, the fluorescence intensity of Si at λ_{em} = 385 nm gradually reduced, and the fluorescence intensity of FITC at λ_{em} = 490 nm increased with the increase of $KMnO_4$ concentration. The fluorescence intensity ratio (F_{385}/F_{490}) was negatively correlated with $KMnO_4$ concentration (Figs. 4(a) and 4(b)). By comparison, $KMnO_4$ effectively quenched the fluorescence of free FITC, which was different from the effect of $KMnO_4$ on the FITC fluorescence in Si-FITC NPs (Fig. S5 in the ESM). This result significantly increased the change of fluorescence intensity ratio, greatly improving the detection sensitivity. With emission mode, the fluorescence of Si in Si-FITC NPs excited by 380 nm was quenched by $KMnO_4$, and the fluorescence of FITC in Si-FITC NPs excited by 490 nm was enhanced by $KMnO_4$ (Fig. S6 in the ESM), indicating that the fluorescence enhancement of FITC was not from the quenched fluorescence of Si. The mechanism of $KMnO_4$ enhancing fluorescence of FITC in Si-FITC NPs requires to be further investigated. The quenching mechanism of Si fluorescence in Si-FITC NPs by $KMnO_4$ was judged by UV–vis absorption spectra and time-resolved fluorescence spectra. When Si-FITC NPs were mixed with $KMnO_4$, the UV–vis absorption peak of FITC and Si did not change, indicating that $KMnO_4$ did not react with Si-FITC NPs (Fig. S7 in the ESM). The fluorescence lifetime of Si-FITC NPs significantly decreased in the presence of $KMnO_4$ (Fig. S8 in the ESM), suggesting that $KMnO_4$ led to the

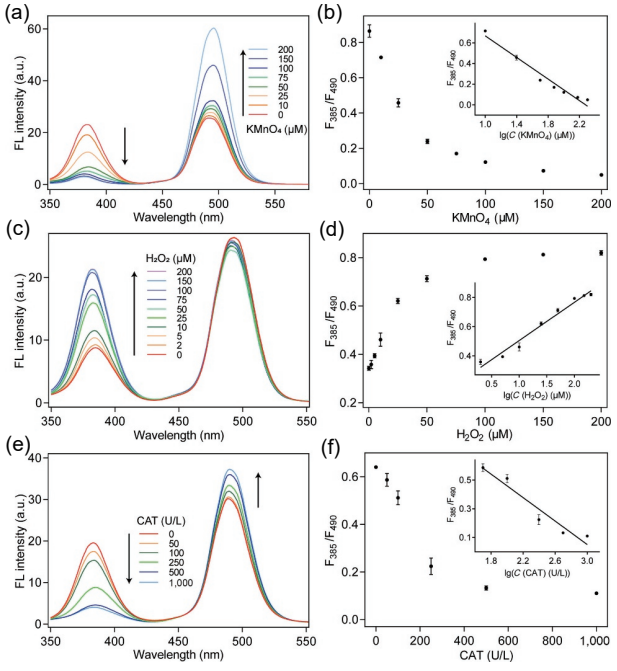

Figure 4 The response of Si-FITC NPs to $KMnO_4$, H_2O_2, and CAT. (a) Synchronous fluorescence spectra and (b) fluorescence intensity ratio of Si-FITC NPs in response to different concentrations of $KMnO_4$. (c) Synchronous fluorescence spectra and (d) fluorescence intensity ratio of Si-FITC NPs treated with 50 μM $KMnO_4$ in response to various concentrations of H_2O_2. (e) Synchronous fluorescence spectra and (f) fluorescence intensity ratio of Si-FITC NPs treated with 50 μM $KMnO_4$ and 100 μM H_2O_2 in the presence of CAT with different concentrations.

dynamic quenching of Si fluorescence. The energy transfer from nanoparticles to $KMnO_4$ may be one of the quenching mechanisms. Due to the redox reaction between H_2O_2 and $KMnO_4$, the reduced fluorescence intensity ratio may be recovered by addition of H_2O_2 (from 0 to 200 μM), and the fluorescence spectra of Si-FITC NPs can be returned to the original state (Fig. 4(c)). The value of F_{385}/F_{490} was positively correlated with the H_2O_2 concentration (Fig. 4(d)).

3.4 Ratiometric immunoassay for SRAS-CoV-2 N protein

CAT is a commonly used labeling enzyme in ELISA, which is effectively catalyze the decomposition of H_2O_2. In our system, H_2O_2 decomposition by CAT reduced the consumption of $KMnO_4$, and the fluorescence of Si in Si-FITC NPs was quenched by excessive $KMnO_4$. To obtain the highest signal-to-noise ratio, the usage of $KMnO_4$ and H_2O_2 was optimized. As shown in Fig. S9 in the ESM, three different $KMnO_4$ concentrations (50, 100, and 200 μM) were selected, and the fluorescence intensity ratio increased with the increase of H_2O_2 concentration. The change in the fluorescence intensity ratio was maximum with 100 μM H_2O_2 and 50 μM $KMnO_4$. Under this condition, a series of CAT concentrations were tested, and the fluorescence spectra showed that the fluorescence of Si was gradually quenched and the FITC fluorescence gradually enhanced. The value of F_{385}/F_{490} negatively correlated with CAT concentration (Fig. 4(e) and 4(f)). Before the immunoassay of N protein, CAT was modified with NHS-biotin for binding with SA to form immunocomplex. To verify the binding efficiency, the biotin-CAT conjugates were separated by SA-coated magnetic beads, and the residual CAT in the supernatant was measured by Si-FITC NPs/$KMnO_4$/H_2O_2 system. The fluorescence intensity ratio of the supernatant was similar to that of the blank group, suggesting that CAT was effectively coupled with biotin (Fig. S10 in the ESM).

During the ELISA process, CAT-linked secondary antibody/reporter antibody/N protein/capture antibody immunocomplexes were formed on microplate (Scheme 1(b)). Then, H_2O_2 and Si-FITC NPs/$KMnO_4$ were added, and CAT catalyzed the decomposition of H_2O_2. Excessive $KMnO_4$ changed the fluorescence intensity ratio of Si-FITC NPs, which was positively correlated with the N protein concentration. The reaction conditions of biotin-CAT with H_2O_2 were further optimized to improve the sensitivity. When the pH value of Tris-HCl was 7, the CAT activity was the highest (Fig. S11 in the ESM). The maximum change in the fluorescence intensity ratio was observed at 30 °C (Fig. S12 in the ESM), and the reaction between CAT and H_2O_2 was completed within 1 h (Fig. S13 in the ESM). Under the optimal conditions, the detection of SARS-CoV-2 N protein was conducted, and there was a good linear relationship between fluorescence intensity ratio and N protein concentration from 0.02 to 50.00 ng/mL (Fig. 5). The detection limit was 0.003 ng/mL (3 SD/slope), which was lower than that of most previous reports (Table S1 in the ESM). In addition, our proposed method had a higher sensitivity than the commercial ELISA kit with a detection limit of 0.057 ng/mL (Fig. S14 in the ESM), which may be explained by the following two reasons: (1) This proposed method used fluorescence as signal, which sensitivity was higher than that of colorimetry (commercial ELISA kit); (2) the sensitivity of ratiometric fluorescence was higher than that of single-emission fluorescence due to self-calibration of ratiometric fluorescence.

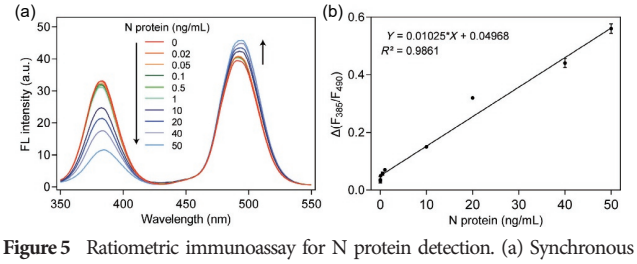

Figure 5 Ratiometric immunoassay for N protein detection. (a) Synchronous fluorescence response of ratiometric ELISA sensor upon N protein with different concentrations. (b) The corresponding linear relationship of the fluorescence intensity ratio and N protein concentration. H_2O_2, 100 μM; $KMnO_4$, 50 μM; $\Delta\lambda$ = 30 nm.

3.5 Detection of N protein in clinical samples

The selectivity of ratiometric fluorescence ELISA for the detection of N protein was studied. N protein specifically reduced the fluorescence intensity ratio, while other proteins had few effects on the ratio when the concentration was 10 times that of N protein (Fig. S15 in the ESM), suggesting that the designed ELISA sensor possessed a high selectivity. To verify the analytical reliability of the designed method in complex biological samples, N protein was spiked into 100% human serum sampled from the First Affiliated Hospital of Shenzhen University. N protein concentrations of 5.32 and 35.18 ng/mL were determined in human serum samples added with 5.00 and 40.00 ng/mL N protein, respectively (Table S2 in the ESM). The recovery rate of samples was 87.95% to 106.40%, and the relative standard deviation was 2.58% to 14.40%, demonstrating that the method can be applied for the detection of N protein in human serum. The detection of clinical samples from COVID-19 and non-COVID-19 patients was conducted using this ratiometric ELISA method. The change in fluorescence intensity ratio was higher in the COVID-19 patient group than in non-COVID-19 patient group (Fig. 6), and the fluorescence intensity ratio change was negatively correlated with Ct value of COVID-19 clinical samples, indicating a good accuracy of this method (Fig. S16 in the ESM). Therefore, the developed immunoassay with a novel ratiometric fluorescent probe possessed a high sensitivity, great selectivity, and great potential in clinical screening of SARS-CoV-2 infections.

4 Conclusions

In summary, we developed a new fluorescent ELISA platform for detection of SARS-CoV-2 N protein. The Si-FITC NPs were prepared via a simple one-pot hydrothermal method using APTES and APTES-FITC as Si co-sources and trisodium citrate as a reducing agent, which can be directly used as a ratiometric probe. The ratiometric probe has an excellent photostability, wide pH stability range, and good anti-interference ability. The Si-FITC NPs/$KMnO_4$ system was applied for ratiometric immunoassay of SARS-CoV-2 N protein, and presented a good linear relationship in the range of 0.02 to 50.00 ng/mL. The limit of detection (0.003 ng/mL) was lower than that of the commercial ELISA kit (0.057 ng/mL). In addition, this method can accurately distinguish COVID-19 patients and non-COVID-19 individuals. It is

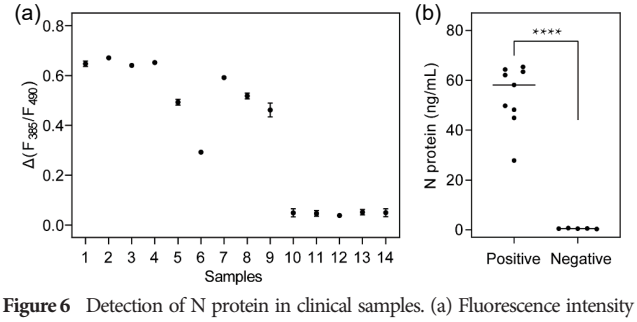

Figure 6 Detection of N protein in clinical samples. (a) Fluorescence intensity ratio change in samples from COVID-19 patients (positive) and non-COVID-19 individuals (negative). (b) Calculated concentration of SARS-CoV-2 N protein in the clinical samples. ****P < 0.000 1.

therefore considered that the ratiometric fluorescent immunoassay is effective for diagnosis of SARS-CoV-2 infections with a high sensitivity and good accuracy. This study not only proposes a novel method for constructing a dual-emitting nanoprobe with a single particle, but also provides a new strategy for ratiometric fluorescence immunoassay, which increases the sensitivity of biomolecule assays.

Acknowledgements

This work was supported by the National Key Research and Development Program of China (No. 2021YFA0910900), the Sino-German rapid response funding call for COVID-19 related research (No. C-0008), the National Natural Science Foundation of China (Nos. 32222044 and 22104147), Shenzhen Municipal Science and Technology Innovation Council (No. RCYX20210609103823046), Youth Innovation Promotion Association CAS (No. 2021359), Natural Science Foundation of Guangdong (Nos. 2018B030306046 amd 2020A1515111130), Guangdong Provincial Key Laboratory of Synthetic Genomics (No. 2019B030301006), Shenzhen Science and Technology Program (No. KQTD20180413181837372), and Shenzhen Outstanding Talents Training Fund.

Ethics declarations

The study protocol was approved by the Ethics Review Committee of Shenzhen Third People's Hospital (No. 2020-010). Written informed consent was obtained from all patients. The study was conducted in accordance with the International Conference on Harmonization Guidelines for Good Clinical Practice, the Declaration of Helsinki and institutional ethics guidelines.

Electronic Supplementary Material: Supplementary material (characterization of Si-FITC NPs (FTIR, HRXPS); stability investigation of Si-FITC NPs (photostability, pH stability, anti-interference ability); stability investigation of free FITC (pH value, $KMnO_4$); quenching mechanism of $KMnO_4$ (UV–vis absorption spectra, fluorescence lifetime decay curves); reaction condition optimization of biotin-CAT with H_2O_2 (pH value, temperature, time); detection of N protein using commercial ELISA Kit; selectivity investigation of assays for SARS-CoV-2 N protein detection; determination results of SARS-CoV-2 N protein in human serum) is available in the online version of this article at https://doi.org/10.1007/s12274-022-5005-z.

References

[1] Zhu, N.; Zhang, D.; Wang, W.; Li, X.; Yang, B.; Song, J.; Zhao, X.; Huang, B.; Shi, W.; Lu, R. et al. A novel coronavirus from patients with pneumonia in China, 2019. *New. Engl. J. Med.* **2020**, *382*, 727–733.

[2] Zhou, P.; Yang, X. L.; Wang, X. G.; Hu, B.; Zhang, L.; Zhang, W.; Si, H. R.; Zhu, Y.; Li, B.; Huang, C. L. et al. A pneumonia outbreak associated with a new coronavirus of probable bat origin. *Nature* **2020**, *579*, 270–273.

[3] Rosenthal, P. J. The importance of diagnostic testing during a viral pandemic: early lessons from novel coronavirus disease (COVID-19). *Am. J. Trop. Med. Hyg.* **2020**, *102*, 915–916.

[4] Yang, Y.; Yang, M.; Yuan, J.; Wang, F.; Wang, Z.; Li, J.; Zhang, M.; Xing, L.; Wei, J.; Peng, L. et al. Laboratory diagnosis and monitoring the viral shedding of SARS-CoV-2 infection. *Innovation (N Y)* **2020**, *1*, 100061.

[5] Wiersinga, W. J.; Rhodes, A.; Cheng, A. C.; Peacock, S. J.; Prescott, H. C. Pathophysiology, transmission, diagnosis, and treatment of coronavirus disease 2019 (COVID-19) a review. *JAMA.* **2020**, *324*, 782–793.

[6] Vogels, C. B. F.; Brito, A. F.; Wyllie, A. L.; Fauver, J. R.; Ott, I. M.; Kalinich, C. C.; Petrone, M. E.; Casanovas-Massana, A.; Muenker, M. C.; Moore, A. J. et al. Analytical sensitivity and efficiency comparisons of SARS-CoV-2 RT-qPCR primer-probe sets. *Nat. Microbiol.* **2020**, *5*, 1299–1305+.

[7] Wang, Y.; Kang, H.; Liu, X.; Tong, Z. Combination of RT-qPCR testing and clinical features for diagnosis of COVID-19 facilitates management of SARS-CoV-2 outbreak. *J. Med. Virol.* **2020**, *92*, 538–539.

[8] Miller, S.; Chiu, C.; Rodino, K. G.; Miller, M. B. Point-counterpoint: should we be performing metagenomic next-generation sequencing for infectious disease diagnosis in the clinical laboratory? *J. Clin. Microbiol.* **2020**, *58*, e01739–19.

[9] Augustine, R.; Hasan, A.; Das, S.; Ahmed, R.; Mori, Y.; Notomi, T.; Kevadiya, B. D.; Thakor, A. S. Loop-mediated isothermal amplification (LAMP): A rapid, sensitive, specific, and cost-effective point-of-care test for coronaviruses in the context of COVID-19 pandemic. *Biology (Basel).* **2020**, *9*, 182.

[10] Lalli, M. A.; Langmade, S. J.; Chen, X.; Fronick, C. C.; Sawyer, C. S.; Burcea, L. C.; Wilkinson, M. N.; Fulton, R. S.; Heinz, M.; Buchser, W. J. et al. Rapid and extraction-free detection of SARS-CoV-2 from saliva by colorimetric reverse-transcription loop-mediated isothermal amplification. *Clin. Chem.* **2021**, *67*, 415–424.

[11] Fozouni, P.; Son, S.; Derby, M. D. d. L.; Knott, G. J.; Gray, C. N.; D'Ambrosio, M. V.; Zhao, C.; Switz, N. A.; Kumar, G. R.; Stephens, S. I. et al. Amplification-free detection of SARS-CoV-2 with CRISPR-Cas13a and mobile phone microscopy. *Cell* **2021**, *184*, 323–333.e9.

[12] Broughton, J. P.; Deng, X.; Yu, G.; Fasching, C. L.; Servellita, V.; Singh, J.; Miao, X.; Streithorst, J. A.; Granados, A.; Sotomayor-Gonzalez, A. CRISPR–Cas12-based detection of SARS-CoV-2. *Nat. biotechnol.* **2020**, *38*, 870–874.

[13] Ding, X.; Yin, K.; Li, Z.; Lalla, R. V.; Ballesteros, E.; Sfeir, M. M.; Liu, C. Ultrasensitive and visual detection of SARS-CoV-2 using all-in-one dual CRISPR-Cas12a assay. *Nat. Commun.* **2020**, *11*, 4711.

[14] Shen, M.; Zhou, Y.; Ye, J.; Al-Maskri, A. A. A.; Kang, Y.; Zeng, S.; Cai, S. Recent advances and perspectives of nucleic acid detection for coronavirus. *J. Pharm. Anal.* **2020**, *10*, 97–101.

[15] Chen, M.; Cui, D.; Zhao, Z.; Kang, D.; Li, Z.; Albawardi, S.; Alsageer, S.; Alamri, F.; Alhazmi, A.; Amer, M. R. et al. Highly sensitive, scalable, and rapid SARS-CoV-2 biosensor based on In_2O_3 nanoribbon transistors and phosphatase. *Nano. Res.* **2022**, *15*, 5510–5516.

[16] Hu, R.; Liao, T.; Ren, Y.; Liu, W.; Ma, R.; Wang, X.; Lin, Q.; Wang, G.; Liang, Y. Sensitively detecting antigen of SARS-CoV-2 by NIR-II fluorescent nanoparticles. *Nano Res.* **2022**, *15*, 7313–7319.

[17] Deeks, J. J.; Dinnes, J.; Takwoingil, Y.; Davenport, C.; Spijker, R.; Taylor-Phillips, S.; Adrianol, A.; Beesel, S.; Dretzkel, J.; di Ruffanol, L. F. et al. Antibody tests for identification of current and past infection with SARS-CoV-2. *Cochrane Db. Syst. Rev.* **2020**, *6*, CD013652.

[18] Liu, W.; Liu, L.; Kou, G.; Zheng, Y.; Ding, Y.; Ni, W.; Wang, Q.; Tan, L.; Wu, W.; Tang, S. et al. Evaluation of nucleocapsid and spike protein-based enzyme-linked immunosorbent assays for detecting antibodies against SARS-CoV-2. *J. Clin. Microbiol.* **2020**, *58*, e00461–20.

[19] Scohy, A.; Anantharajah, A.; Bodeus, M.; Kabamba-Mukadi, B.; Verroken, A.; Rodriguez-Villalobos, H. Low performance of rapid antigen detection test as frontline testing for COVID-19 diagnosis. *J. Clin. Virol.* **2020**, *129*, 104455.

[20] Dinnes, J.; Deeks, J. J.; Adriano, A.; Berhane, S.; Davenport, C.; Dittrich, S.; Emperador, D.; Takwoingi, Y.; Cunningham, J.; Beese, S. et al. Rapid, point-of-care antigen and molecular-based tests for diagnosis of SARS-CoV-2 infection (Review). *Cochrane Db. Syst. Rev.* **2020**, *8*, CD013705.

[21] Reen, D. J. Enzyme-linked immunosorbent assay (ELISA). *Methods. Mol. Bioll.* **1994**, *32*, 461–466.

[22] Zhang, D.; Li, W.; Ma, Z.; Han, H. Improved ELISA for tumor marker detection using electro-readout-mode based on label

triggered degradation of methylene blue. *Biosens. Bioelectron.* **2019**, *126*, 800–805.

[23] Wu, L.; Li, G.; Xu, X.; Zhu, L.; Huang, R.; Chen, X. Application of nano-ELISA in food analysis: Recent advances and challenges. *Trac-Trend Anal. Chem.* **2019**, *113*, 140–156.

[24] de la Rica, R.; Stevens, M. M. Plasmonic ELISA for the ultrasensitive detection of disease biomarkers with the naked eye. *Nat. Nanotechnol.* **2012**, *7*, 821–824.

[25] Luo, Q.; Wang, H.; Yin, X.; Wang, L. Hydrophilic perovskite microdisks with excellent stability and strong fluorescence for recyclable temperature sensing. *Sci. China. Mater.* **2019**, *62*, 1065–1070.

[26] Liang, Y.; Huang, X.; Yu, R.; Zhou, Y.; Xiong, Y. Fluorescence ELISA for sensitive detection of ochratoxin A based on glucose oxidase-mediated fluorescence quenching of CdTe QDs. *Anal. Chim. Acta.* **2016**, *936*, 195–201.

[27] Chu, B.; Song, B.; Ji, X.; Su, Y.; Wang, H.; He, Y. Fluorescent silicon nanorods-based ratiometric sensors for long term and real-time measurements of intracellular pH in live cells. *Anal. Chem.* **2017**, *89*, 12152–12159.

[28] Zhai, X.; Song, B.; Chu, B.; Su, Y.; Wang, H.; He, Y. Highly fluorescent, photostable, and biocompatible silicon theranostic nanoprobes against Staphylococcus aureus infections. *Nano Res.* **2018**, *11*, 6417–6427.

[29] Guo, D.; Ji, X.; Peng, F.; Zhong, Y.; Chu, B.; Su, Y.; He, Y. Photostable and biocompatible fluorescent silicon nanoparticles for imaging-guided co-delivery of siRNA and doxorubicin to drug-resistant cancer cells. *Nano-micro. Lett.* **2019**, *11*, 27.

[30] Sun, J.; Hu, T.; Chen, C.; Zhao, D.; Yang, F.; Yang, X. Fluorescence immunoassay system via enzyme-enabled in situ synthesis of fluorescent silicon nanoparticles. *Anal. Chem.* **2016**, *88*, 9789–9795.

[31] Chen, C.; Zhao, D.; Wang, B.; Ni, P.; Jiang, Y.; Zhang, C.; Yang, F.; Lu, Y.; Sun, J. Alkaline phosphatase-triggered in situ formation of silicon-containing nanoparticles for a fluorometric and colorimetric dual-channel immunoassay. *Anal. Chem.* **2020**, *92*, 4639–4646.

[32] Wang, J.; Liu, X.; Huang, L.; Jin, J.; Jiang, C.; Li, D.; Wen, H.; Hu, J. Controllable and robust dual-emissive quantum dot nanohybrids as inner filter-based ratiometric probes for visualizable melamine detection. *Nanoscale* **2020**, *12*, 4562–4572.

[33] Zhang, J.; Qian, J.; Mei, Q.; Yang, L.; He, L.; Liu, S.; Zhang, C.; Zhang, K. Imaging-based fluorescent sensing platform for quantitative monitoring and visualizing of fluoride ions with dual-emission quantum dots hybrid. *Biosens. Bioelectron.* **2019**, *128*, 61–67.

[34] Zhang, Y.; Guo, S.; Jiang, Z.; Mao, G.; Ji, X.; He, Z. Rox-DNA functionalized silicon nanodots for ratiometric detection of mercury ions in live cells. *Anal. Chem.* **2018**, *90*, 9796–9804.